



# H<sub>2</sub>-H<sub>2</sub>O immiscibility in Earth's upper mantle

Kirill Vlasov<sup>1,2</sup> · Andreas Audétat<sup>1</sup> · Hans Keppler<sup>1</sup>

Received: 16 February 2023 / Accepted: 24 May 2023 / Published online: 5 June 2023  
© The Author(s) 2023

## Abstract

Immiscibility between water and hydrogen-rich fluids may be responsible for the formation of super-reduced mineral assemblages and for the early oxidation of Earth's upper mantle. In the current study, we present new data on the critical curve in the H<sub>2</sub>-H<sub>2</sub>O system to 1400 °C and 4 GPa. We utilized a synthetic fluid inclusion method to trap fluids at high P–T conditions within quartz and olivine crystals. Experiments were performed in a piston-cylinder type apparatus, employing a double-capsule technique. The inner capsule contained the crystal and fluids of interest, while the outer served as oxygen fugacity buffer, maintaining  $f(O_2)$  at the iron-wüstite (Fe-FeO) equilibrium. Our results suggest that below ~2.5 GPa, the critical curve has a mostly linear slope of 200 °C/GPa, while at more elevated pressure it becomes significantly steeper (400 °C/GPa). This implies that in most of the modern, reduced upper mantle, water and hydrogen are immiscible, while localized heating events, such as rising plumes, may close the miscibility gap. The steep increase of the critical curve at high pressure observed in this study implies that even for very hot geotherms in the early Archean or the late Hadean, H<sub>2</sub>-H<sub>2</sub>O immiscibility likely occurred in the deeper parts of the upper mantle, thus making a plausible case for rapid H<sub>2</sub> loss as a mechanism of early mantle oxidation. To constrain the geochemical fingerprint of this process, we performed a series of element partitioning experiments to unravel how the H<sub>2</sub>-H<sub>2</sub>O unmixing may affect element transfer. Noble gases such as Xe as well as methane are preferentially incorporated in the hydrogen-rich phase, with a Xe<sub>H<sub>2</sub>O</sub>/Xe<sub>H<sub>2</sub></sub> ratio of ~8. This partitioning pattern may, for example, explain the underabundance of Xe isotopes produced by fission of Pu in the mantle. These Xe isotopes may have been removed by a primordial H<sub>2</sub>-H<sub>2</sub>O unmixing event during the early stages of planetary evolution.

**Keywords** Hydrogen · Mantle fluids · Xenon · Piston-cylinder experiments · Super-reducing mineral assemblages · Degassing · Immiscibility · Mantle oxidation · Archean

## Introduction

Hydrogen speciation in the interior of planets depends on oxidation state. For example, in Earth's uppermost lithospheric mantle, oxygen fugacity  $f(O_2)$  ranges from +2 to -3 log units relative to the quartz-fayalite-magnetite buffer ( $\Delta QFM$ ) (Ballhaus 1993; Frost and McCammon 2008). Such conditions are typically considered as relatively oxidizing for the mantle, with the primary hydrogen species

being molecular H<sub>2</sub>O or bound hydroxyl groups (OH<sup>-</sup>). At greater depths and pressures, exceeding 200 km and 5–7 GPa, respectively, oxygen fugacity evolves towards more reducing values, approaching the iron-wüstite (IW) buffer with relatively little further deviation (1–1.5 log units) (Frost and McCammon 2008). As the environment becomes more reducing, the fraction of water in fluids decreases and molecular hydrogen H<sub>2</sub> as well as methane CH<sub>4</sub> become the primary H-species. Recent studies indicate that in the more reduced parts of the mantle, H<sub>2</sub> may not only be present in a free fluid phase, but also as dissolved species in minerals and melts (Hirschmann et al. 2012; Yang et al. 2016).

While the depth-dependent fugacity profile described above holds true for the majority of the contemporary mantle environments, there may be local, though geologically significant exceptions. Enigmatic super-reducing domains contain mineral assemblages recording  $\log f(O_2)$  far below the IW buffer. A characteristic phase, most commonly cited as

Communicated by Dante Canil.

✉ Kirill Vlasov  
kirill.vlasov@bristol.ac.uk

<sup>1</sup> Bayerisches Geoinstitut, Universität Bayreuth, 95440 Bayreuth, Germany

<sup>2</sup> Present Address: School of Earth Sciences, University of Bristol, Wills Memorial Building, Queens Road, Bristol BS8 1RJ, UK

an indicator of such super-reducing environments, is moissanite (SiC). The formation of SiC requires extremely low oxygen fugacities with  $\log f(O_2)$  approximately 5–8 units below the IW buffer (e.g. Golubkova et al. 2016; Ulmer et al. 1998). In the past, it was sometimes questioned, whether the moissanite in mantle samples is actually a natural phase or a synthetic contamination. However, SiC has now been discovered in situ in a wide range of geological settings, including kimberlites and lamproites (Kaminsky 2012; Shiryaev et al. 2011), ophiolites (Golubkova et al. 2016; Pujol-Solà et al. 2018; Trumbull et al. 2009), alkaline basalt tuffs (Dobrzhinetskaya et al. 2018), and syenites (Nazzareni et al. 2019). In such super-reducing mineral assemblages, moissanite is commonly associated with native iron, silicon, various alloys, wüstite, phosphides and nitrides. Traditionally, these phases were thought to originate at great depth (< 200–250 km), where conditions may perhaps be locally more reducing. While this may be so in some cases, Bali et al. (2013) suggested that super-reducing conditions can emerge even at 100–200 km depth from the percolation of hydrogen-rich fluids, produced via unmixing in the  $H_2$ - $H_2O$  system.

At present, super-reducing domains are uncommon, since Earth's upper mantle is quite oxidized and comparatively cold (e.g. Abbott et al. 1994; Herzberg et al. 2010). However, at the dawn of the Archean and before, its oxidation and thermal state may have been dramatically different. This is especially true for the first two hundred million years of Earth's history. During and immediately after core formation, as indicated by existing models (Rubie et al. 2011), Earth's interior likely was very reduced, with  $f(O_2)$  being several log units below the IW buffer. Throughout this stage, our planet, as well as Mars and Venus, may have had a hydrogen-rich atmosphere, supported by magma ocean outgassing (Lammer et al. 2018). However, for Earth, the upper mantle remained reduced at most for about 200 Myr. Based on the oxygen fugacity estimates of Trail et al. (2011), the redox state of the upper mantle was already close to that prevailing today at 4350 Myr before present. An early oxidation of the upper mantle has been noted for Mars as well, suggesting that it may be a common phase of the evolution of the terrestrial planets (Tuff et al. 2013).

The short timescale of the oxidation event points towards a fast process responsible for it. While the exact mechanism is still under discussion (Armstrong et al. 2019; Williams et al. 2012), the emergence of the miscibility gap between water and hydrogen upon cooling of the mantle was considered as a plausible cause (Bali et al. 2013). Global degassing of a highly mobile and buoyant  $H_2$ -rich phase could have rapidly oxidized the remaining mantle. Moreover, it would certainly have affected the mantle abundances of other elements, especially noble gases, such as Xe or Ar. An early loss of radiogenic  $^{129}\text{Xe}$  and of Xe isotopes produced by

Pu fission has indeed been reported (Kunz et al. 1998), but linking it to  $H_2$ - $H_2O$  unmixing requires the knowledge of partition coefficients between water and hydrogen at reduced upper mantle conditions that are currently unknown.

In this paper, we present new data on the position of the critical curve in the  $H_2$ - $H_2O$  system from 1 to 4 GPa, which approximately doubles the data coverage from the previous study of Bali et al. (2013). Moreover, we report the first experiments on element partitioning between the two coexisting fluid phases. The data will be applied to better understand the formation of super-reducing domains, the processes of mantle degassing during the first stages of Earth's history, and the causes for the rapid loss of Xe from the early Earth.

## Experimental methods

### Starting material and capsule preparation

For trapping fluid inclusions, small cylinders (diameter 2.2 mm, length 1 mm) were cut out of bulk pieces of clear, natural quartz (Brazil), natural olivine (Dac Lac, Vietnam), and synthetic forsterite. Cylinders were thermally cracked by heating them to 1000 °C in a furnace and then immediately dropping them into distilled water. For experiments at pressures below 2.5 GPa, quartz was used to trap the inclusions, while forsterite was chosen for higher pressures. This change of the host crystal is necessary because of the quartz–coesite transition, which transforms a single crystal of quartz into a polycrystalline aggregate of coesite unsuitable for trapping inclusions (Lathe et al. 2005).

A double-capsule technique (for detailed discussion, see Chou 1987) was used to buffer the oxygen fugacity at the Fe-FeO equilibrium, to contain hydrogen during the experiment, and to protect the crystals from Fe contamination. In several early test runs for measuring the critical curve, the forsterite crystal core was loaded directly into the buffering mixture (Fe + FeO), without the inner capsule. We found out that with olivine, this method cannot be utilized at temperatures above 1100–1200 °C in the selected pressure range due to the precipitation of Fe-rich brucite and pure iron that complicate the analysis of  $H_2$  and  $H_2O$  in the fluid inclusions. Two low-temperature (900 and 1000 °C) 3 GPa samples produced in this way were used in the present study, as they show no signs of the aforementioned additional solid phases. For the rest of the experiments in this study, a double-capsule was used, regardless of the crystal type. Depending on the purpose of the run—locating the critical curve or element partitioning experiments—only the contents of the inner capsule differed, with the rest of the assembly remaining unchanged and being generally similar to the technique utilized by Bali et al. (2013).

For experiments to determine the position of the critical curve, the inner Pt<sub>95</sub>Rh<sub>5</sub> capsule (outer diameter 2.5 mm, inner diameter 2.3 mm, length 5–6 mm) contained only the crystal cylinder, with the rest being filled up with ultrapure water (Millipore,  $\sigma = 0.06 \mu\text{S}$ ) (Fig. 1a). For element partitioning experiments the capsule was filled from bottom to top in the following sequence: A layer of Ca(OH)<sub>2</sub> (Merck, > 96%), XeF<sub>2</sub> crystals (Alfa Aesar, 99.5%), a layer of synthetic diopside-glass powder doped with about 25 trace elements at the 0.5–1 wt. % level (sample MORB2-2D2, Table S8 in supplementary file 1, Rustioni et al. 2019), Au foil (24 carat, Noris Blattgoldfabrik), the crystal cylinder, and ~ 10  $\mu\text{l}$  of water containing 1000 ppm of both Rb and Cs (Fig. 1b). The solution, replacing pure water in this type of capsule, was prepared by the addition of RbCl (chemPUR, 99.9%) and CsCl (chemPUR, 99.99%) to the distilled water. Here, Xe and Rb/Cs were introduced for use as internal standards during later analysis, assuming that they would be incorporated primarily into the H<sub>2</sub> and H<sub>2</sub>O phases, respectively. While adding Xe in the form of the solid XeF<sub>2</sub> is convenient, the release of fluorine during the decomposition of XeF<sub>2</sub> into Xe and F<sub>2</sub> upon heating is undesired. The Ca(OH)<sub>2</sub> layer binds this excess fluorine in the form of CaF<sub>2</sub>. This prevents the formation of HF as an unwanted component in the fluid. The thin gold membrane separated H<sub>2</sub>O from XeF<sub>2</sub> during capsule preparation, in order to avoid premature decomposition by hydrolysis ( $\text{XeF}_2 + \text{H}_2\text{O} \rightarrow \text{Xe} + 0.5\text{O}_2 + 2\text{HF}$ ). After the addition of the crystal and water or solution the capsule was arc-welded. Following the welding procedure, the inner capsule was

inserted into the outer capsule machined of Fe (GoodFellow, 99.8%, outer diameter 5 mm, inner diameter 3 mm, length 10 mm), together with a mixture of distilled water and FeO (Sigma-Aldrich, 99.7%) that ensured Fe-FeO buffer conditions (Fig. 1c). This outer capsule was closed by inserting the lid and was mechanically sealed on compression.

### Piston-cylinder experiments

Experiments were carried out in an end-loaded piston-cylinder apparatus using 1/2" talc/pyrex assemblies with a tapered graphite heater. A friction correction of 18% was applied to the nominal pressure, according to a calibration by the quartz-coesite transition at 790 °C (Bose and Ganguly 1995). Temperature was measured with S-type thermocouples (Pt–Pt<sub>90</sub>Rh<sub>10</sub>) below 1300 °C, and with D-type thermocouples (W<sub>97</sub>Re<sub>3</sub>–W<sub>75</sub>Re<sub>25</sub>) at higher temperatures. To ensure minimal secondary alteration and recrystallization of the inclusions, run durations varied between 24 and 5 h (for exact run durations see Table 1). At the end of the run, 25–30% of the pressure was released over the period of 10–30 min, followed by several hours of continuous decompression to ambient conditions. Simultaneously with the initial pressure release, the runs were quenched at ~ 100 °C/minute. According to previous research performed at similar conditions, this approach allows to preserve inclusions and minimizes secondary changes (Bali et al. 2013; Tingle et al. 1992). For pressures  $\geq 3$  GPa, the decompression P–T paths were slightly adjusted to avoid ice formation, with an

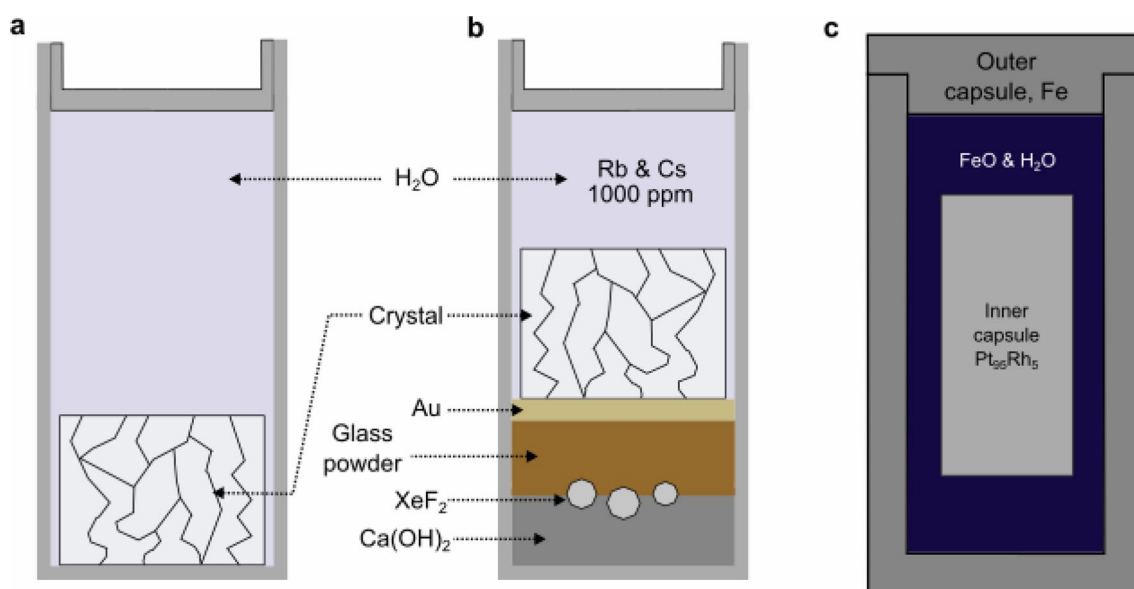


**Fig. 1** Design of the double-capsules used for experiments. **a** and **b** show details of inner capsules, **c** shows the entire double-capsule. For experiments used to locate the critical curve, inner capsules of type

**a** were used, while type **b** was used for element partitioning experiments. Diagrams are not to scale

**Table 1** List of experiments performed to determine the position of H<sub>2</sub>-H<sub>2</sub>O critical curve

Experiment	Pressure, GPa	Temperature, °C	Run duration, h	Crystal	Double capsule	Run products description
KVH01	3	900	24	Olivine (Dac Lac, Vietnam)	–	H <sub>2</sub> , H <sub>2</sub> O, H <sub>2</sub> + H <sub>2</sub> O*
KVH02	3	1000	24	Olivine (Dac Lac, Vietnam)	–	H <sub>2</sub> , H <sub>2</sub> O, H <sub>2</sub> + H <sub>2</sub> O
KVH03	3	1100	24	Olivine (Dac Lac, Vietnam)	–	H <sub>2</sub> , H <sub>2</sub> O, H <sub>2</sub> + H <sub>2</sub> O
KVH04	3	1200	24	Olivine (Dac Lac, Vietnam)	–	H <sub>2</sub> + H <sub>2</sub> O + Fe + FeO + Brc
KVH05	3	1250	24	Olivine (Dac Lac, Vietnam)	–	H <sub>2</sub> + H <sub>2</sub> O + Fe + FeO + Brc
KVH06	3	1300	24	Olivine (Dac Lac, Vietnam)	–	H <sub>2</sub> + H <sub>2</sub> O + Fe + FeO + Brc
KVH07	3	1250	22	Olivine (Dac Lac, Vietnam)	–	H <sub>2</sub> + H <sub>2</sub> O + Fe + FeO + Brc
KVH08	3.5	1100	22	Olivine (Dac Lac, Vietnam)	–	H <sub>2</sub> , H <sub>2</sub> O, H <sub>2</sub> + H <sub>2</sub> O
KVH09	3.5	1200	22	Olivine (Dac Lac, Vietnam)	–	H <sub>2</sub> + H <sub>2</sub> O + Fe + FeO + Brc
KVH10	3.5	1300	23	Olivine (Dac Lac, Vietnam)	–	H <sub>2</sub> + H <sub>2</sub> O + Fe + FeO + Brc
KVH11	4	1200	20	Olivine (Dac Lac, Vietnam)	–	H <sub>2</sub> + H <sub>2</sub> O + Fe + FeO + Brc
KVH13	3.5	1300	20	Olivine (Dac Lac, Vietnam)	–	H <sub>2</sub> + H <sub>2</sub> O + Fe + FeO + Brc
KVH14	4	1400	20	Olivine (Dac Lac, Vietnam)	–	Fe + FeO
KVH15	3	1200	24	Olivine (Dac Lac, Vietnam)	–	H <sub>2</sub> + H <sub>2</sub> O + Fe + FeO + Brc
KVH16	3	1175	24	Olivine (Dac Lac, Vietnam)	–	H <sub>2</sub> + H <sub>2</sub> O + Fe + FeO
KVH18	3	1225	24	Olivine (Dac Lac, Vietnam)	–	H <sub>2</sub> + H <sub>2</sub> O + Fe + FeO + Brc
KVH19	3.5	1200	21	Synthetic forsterite	+	H <sub>2</sub> , H <sub>2</sub> O, H <sub>2</sub> + H <sub>2</sub> O
KVH20	3.5	1250	21	Synthetic forsterite	+	H <sub>2</sub> , H <sub>2</sub> O, H <sub>2</sub> + H <sub>2</sub> O
KVH21	3.5	1350	21	Synthetic forsterite	+	H <sub>2</sub> , H <sub>2</sub> O, H <sub>2</sub> + H <sub>2</sub> O, Brc
KVH22	4	1300	21	Synthetic forsterite	+	H <sub>2</sub> , H <sub>2</sub> O, H <sub>2</sub> + H <sub>2</sub> O
KVH30	3	1150	20	Synthetic forsterite	+	H <sub>2</sub> , H <sub>2</sub> O, H <sub>2</sub> + H <sub>2</sub> O
KVH32	2.5	1100	22	Synthetic forsterite	+	H <sub>2</sub> + H <sub>2</sub> O
KVH33	2.5	1000	22	Synthetic forsterite	+	H <sub>2</sub> , H <sub>2</sub> O, H <sub>2</sub> + H <sub>2</sub> O
KVH35	2.5	950	24	Synthetic forsterite	+	H <sub>2</sub> , H <sub>2</sub> O, H <sub>2</sub> + H <sub>2</sub> O
KVH36	2.5	1050	24	Synthetic forsterite	+	H <sub>2</sub> + H <sub>2</sub> O
KVH37	2.5	1050	21	Synthetic forsterite	+	H <sub>2</sub> + H <sub>2</sub> O
KVH38	2.5	950	24	Synthetic forsterite	+	H <sub>2</sub> , H <sub>2</sub> O, H <sub>2</sub> + H <sub>2</sub> O
KVH39	2.5	1050	24	Synthetic forsterite	+	H <sub>2</sub> + H <sub>2</sub> O
KVH41	2.5	1150	21	Synthetic forsterite	+	H <sub>2</sub> + H <sub>2</sub> O
KVH42	2.5	900	24	Synthetic forsterite	+	H <sub>2</sub> , H <sub>2</sub> O, H <sub>2</sub> + H <sub>2</sub> O
KVH43	2	900	24	Quartz (Brazil)	+	H <sub>2</sub> + H <sub>2</sub> O
KVH44	2	800	24	Quartz (Brazil)	+	H <sub>2</sub> , H <sub>2</sub> O, H <sub>2</sub> + H <sub>2</sub> O
KVH45	2	950	24	Quartz (Brazil)	+	H <sub>2</sub> + H <sub>2</sub> O
KVH46	2	850	24	Quartz (Brazil)	+	H <sub>2</sub> , H <sub>2</sub> O, H <sub>2</sub> + H <sub>2</sub> O
KVH47	2	850	24	Quartz (Brazil)	+	H <sub>2</sub> , H <sub>2</sub> O, H <sub>2</sub> + H <sub>2</sub> O
KVH48	2	850	19	Quartz (Brazil)	+	H <sub>2</sub> , H <sub>2</sub> O, H <sub>2</sub> + H <sub>2</sub> O
KVH49	2	900	18	Quartz (Brazil)	+	H <sub>2</sub> + H <sub>2</sub> O
KVH50	2.5	1050	21	Synthetic forsterite	+	H <sub>2</sub> + H <sub>2</sub> O
KVH51	2.5	1100	19	Synthetic forsterite	+	H <sub>2</sub> + H <sub>2</sub> O
KVH52	2.5	1150	19	Synthetic forsterite	+	H <sub>2</sub> + H <sub>2</sub> O
KVH53	3.5	900	12	Synthetic forsterite	+	H <sub>2</sub> , H <sub>2</sub> O, H <sub>2</sub> + H <sub>2</sub> O
KVH54	3.5	1200	14	Synthetic forsterite	+	H <sub>2</sub> , H <sub>2</sub> O, H <sub>2</sub> + H <sub>2</sub> O
KVH55	3.5	1300	9	Synthetic forsterite	+	H <sub>2</sub> , H <sub>2</sub> O, H <sub>2</sub> + H <sub>2</sub> O
KVH56	4	1250	10	Synthetic forsterite	+	H <sub>2</sub> , H <sub>2</sub> O, H <sub>2</sub> + H <sub>2</sub> O, Brc
KVH57	3.5	1350	7	Synthetic forsterite	+	H <sub>2</sub> , H <sub>2</sub> O, H <sub>2</sub> + H <sub>2</sub> O, Brc
KVH60	3	1250	10	Synthetic forsterite	+	H <sub>2</sub> + H <sub>2</sub> O
KVH62	1.5	650	24	Quartz (Brazil)	+	H <sub>2</sub> , H <sub>2</sub> O, H <sub>2</sub> + H <sub>2</sub> O
KVH63	1.5	700	24	Quartz (Brazil)	+	H <sub>2</sub> , H <sub>2</sub> O, H <sub>2</sub> + H <sub>2</sub> O
KVH64	1.5	750	24	Quartz (Brazil)	+	H <sub>2</sub> + H <sub>2</sub> O

Table 1 (continued)

Experiment	Pressure, GPa	Temperature, °C	Run duration, h	Crystal	Double capsule	Run products description
KVH65	1	750	24	Quartz (Brazil)	+	H <sub>2</sub> + H <sub>2</sub> O
KVH66	1	700	24	Quartz (Brazil)	+	H <sub>2</sub> + H <sub>2</sub> O
KVH67	1	650	24	Quartz (Brazil)	+	H <sub>2</sub> + H <sub>2</sub> O
KVH68	1	600	24	Quartz (Brazil)	+	H <sub>2</sub> , H <sub>2</sub> O, H <sub>2</sub> + H <sub>2</sub> O
KVH69	2	750	24	Quartz (Brazil)	+	H <sub>2</sub> , H <sub>2</sub> O, H <sub>2</sub> + H <sub>2</sub> O
KVH70	2.5	1000	19	Synthetic forsterite	+	H <sub>2</sub> , H <sub>2</sub> O, H <sub>2</sub> + H <sub>2</sub> O
KVH71	3	1200	10	Synthetic forsterite	+	H <sub>2</sub> , H <sub>2</sub> O, H <sub>2</sub> + H <sub>2</sub> O
KVH72	3.5	1300	5	Synthetic forsterite	+	H <sub>2</sub> , H <sub>2</sub> O, H <sub>2</sub> + H <sub>2</sub> O, Brc
KVH73	4	1300	5	Synthetic forsterite	+	H <sub>2</sub> , H <sub>2</sub> O, H <sub>2</sub> + H <sub>2</sub> O, Brc

\*H<sub>2</sub> refers to fluid inclusions containing nearly pure hydrogen, H<sub>2</sub>O refers to nearly pure water inclusions, H<sub>2</sub> + H<sub>2</sub>O are mixed water and hydrogen inclusions, Brc is newly formed brucite, Fe are newly formed particles of Fe metal and FeO—newly formed wüstite

Experiments performed without the double-capsule technique were not used to constrain the critical curve, except for cases specifically mentioned in the text

addition of a low temperature heating step (~ 50–75 °C, max time=2 h) during the final pressure release.

### Sample preparation and Raman investigation

Capsules were cut open after the runs, crystals retrieved, mounted in epoxy resin and doubly polished to a thickness of 100–200 µm. Run products were initially investigated and inclusions were mapped out with a Leica DMLP polarization microscope with objectives ranging from 5× to 50×. Photographs were taken with a Canon EOS D60 camera, mounted on the microscope. Raman spectra of coexisting fluid phases were collected with a Horiba Labram 800 HR UV confocal Raman spectrometer using the 514 nm line of an argon laser at 200 mW output power, a 1800 mm<sup>-1</sup> grating, a two-dimensional CCD detector, and a confocal pinhole of 100 µm with a 50× long-distance objective.

### LA-ICP-MS analyses

Prior to the LA-ICP-MS measurements, fluid inclusions were selected under the microscope, photographed, and the presence of H<sub>2</sub> and H<sub>2</sub>O-rich phases were confirmed with Raman spectroscopy. LA-ICP-MS analyses were performed with a 193 nm ArF Excimer laser ablation unit (GeolasPro system, Coherent, USA) connected to an Elan DRC-e quadrupole ICP-MS (Perkin Elmer, Canada). The sample chamber was flushed with He at 0.4 l/min, to which 5 ml/min of H<sub>2</sub> was added on the way to the ICP-MS machine. Inclusions and standards were ablated with a repetition rate of 10 Hz, with the energy for standards being 90 mJ and for the inclusions 180 mJ. Laser diameter varied based on the size of the inclusion from 8 to 25 µm. NIST SRM 610 glass was used as external standard for all analyzed elements except for Xe, for which a separate glass standard was prepared as detailed

below. Analyzed isotopes were <sup>131</sup>Xe, <sup>132</sup>Xe, <sup>85</sup>Rb, <sup>7</sup>Li, <sup>11</sup>B, <sup>27</sup>Al, <sup>90</sup>Zr, <sup>133</sup>Cs.

As there are no commercially available EPMA or ICP-MS standards for Xe, a new reference material was synthesized. A Xe-bearing glass was produced from a mixture of XeF<sub>2</sub> and powdered natural Armenian obsidian (OA-1; Wu et al. 2022) as starting materials. Xe was added as XeF<sub>2</sub> to yield a concentration of 1 wt.% Xe (Schmidt and Keppler 2002; Shibata et al. 1998). Those compounds were mixed, loaded into a Pt capsule, and heated for 1 h at 1500 °C and 2 GPa in a piston-cylinder apparatus (½” talc/pyrex assembly) and quenched. Optical examination showed no inhomogeneity.

Although Xe, Rb and Cs were originally added to the fluid to serve as internal standard to quantify the signals obtained from H<sub>2</sub>-rich and H<sub>2</sub>O-rich inclusions, respectively, quantification of the H<sub>2</sub>-rich inclusions turned out to be impractical. The results will thus be discussed solely based on relative and absolute signal intensities without any use of internal standards.

## Results

### Position of the critical curve in the H<sub>2</sub>-H<sub>2</sub>O system

Fluid inclusion-capturing experiments were performed for 30 individual pressure–temperature conditions to investigate the location of critical curve in the H<sub>2</sub>-H<sub>2</sub>O system from 1 to 4 GPa (Fig. 2, Table 1). Three types of inclusions can be observed in the samples: Darker, nearly pure H<sub>2</sub> inclusions with strong optical contrast to the host crystal, and lighter H<sub>2</sub>O-rich inclusions with weak optical contrast, as well as inclusions containing both phases at the same time.

Depending on the phase assemblages present in the inclusions, two distinctively different groups of experimental run



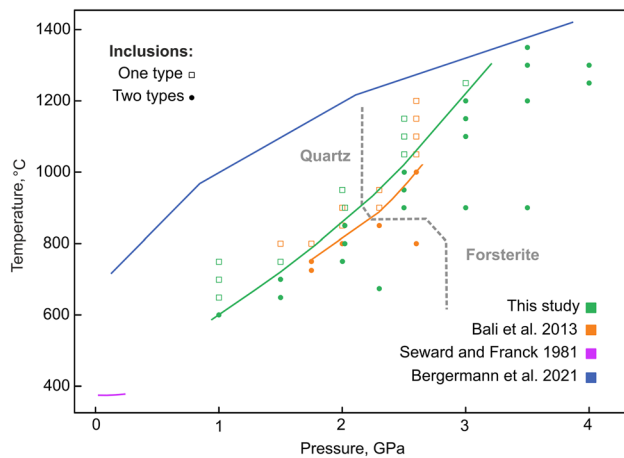


**Fig. 2** Location of the critical curve in the  $\text{H}_2\text{-H}_2\text{O}$  system (green line) according to our experimental data (green symbols). Open squares—only mixed water-hydrogen inclusions are present (full miscibility), filled circles indicate the presence of pure water and pure hydrogen inclusions (immiscibility). The critical curve from Bali et al. (2013) is plotted as orange line with their experimental data being symbols of the same color. The lavender line is a critical curve established by Seward and Franck (1981) and the blue line is a critical curve from a recent computational (Gibbs-ensemble Monte Carlo simulations) study by Bergermann et al. (2021). The dashed, dark grey line separates experiments performed with quartz versus ones performed with olivine, both in this work and in (Bali et al. 2013)

products can be identified. The first group, produced at lower temperatures, contains all three types of inclusions—with nearly pure  $\text{H}_2$ ,  $\text{H}_2\text{O}$ , and their mixture. Following Bali et al. (2013), we interpret this as entrapment within the region of  $\text{H}_2\text{-H}_2\text{O}$  immiscibility (Fig. 3a). The second group, synthesized at higher temperatures, contains only mixed  $\text{H}_2\text{-H}_2\text{O}$  inclusions which we interpret as evidence for full miscibility between those two components at entrapment conditions (Fig. 3b).

Pure liquid water inclusions without any additional phases are observed only in samples synthesized at pressures above  $\sim 2.5$  GPa. Below this value (e.g. supplementary file 2, Figure S1a,c,e), the change in fluid density during cooling causes nucleation of a water vapour bubble. This vapour bubble commonly contains trace amounts of hydrogen since the solubility of hydrogen in water increases as the critical curve is approached from within the immiscibility region. At pressures  $< 2$  GPa, the temperature range with notable  $\text{H}_2$  solubility appears to be larger ( $\sim 100$  °C or even more) than at higher pressures, as indicated by detectable amounts of hydrogen in water inclusions (Fig. 3a). The fluid inclusions in Fig. 3a were synthesized in quartz at 1.5 GPa and 800 °C, i.e., at conditions close to critical curve, but still in the immiscibility region. Two phases can be seen in the water-rich inclusion: liquid water with minor amounts of dissolved hydrogen (blue spectrum), and water vapour (orange spectrum), with a weak peak of gaseous hydrogen.

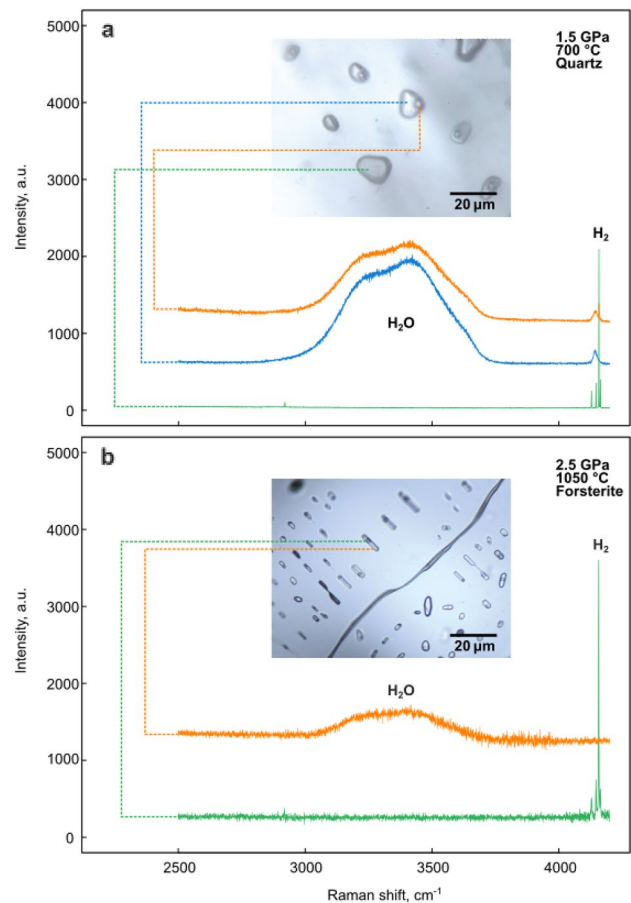


**Fig. 3** Synthetic fluid inclusions formed **a** in quartz at 1.5 GPa and 700 °C, with Raman spectra of the vapor bubble in a water-rich inclusion shown in orange, liquid water in blue, and hydrogen gas in green, and **b** in synthetic forsterite at 2.5 GPa and 1050 °C, with Raman spectra of water shown in orange, and of hydrogen in green. The spectra in Figure **b** were baseline-corrected, the image of inclusions in the same figure is a combination of two photographs made at different focal depths

No dissolved hydrogen was detected in inclusions containing a water phase at higher pressures than 2 GPa. Occasionally, metastable water inclusions synthesized in the immiscibility region at pressures  $< 2.5$  GPa were observed to nucleate a gas phase, triggered by laser ablation of nearby inclusions or upon laser irradiation during Raman analysis. In general, the density of water is relatively constant along the immiscibility curve from 1.5 to 3 GPa (Pitzer and Sterner 1994); it ranges from  $1.02 \text{ g/cm}^3$  at 1.5 GPa and 700 °C to  $1.07 \text{ g/cm}^3$  at 3 GPa and 1200 °C (the highest temperatures at which immiscibility is observed at a given pressures).

Inclusions where  $\text{H}_2$  gas is the dominant or only detectable phase are typically larger, compared to the size of mixed and pure water inclusions. According to Raman measurements, they appear to be either completely free from  $\text{H}_2\text{O}$  or they contain only a thin coating of water along the walls of

the inclusion. They also tend to be more resistant to recrystallization in our experiments, due to the extremely low solubility of major rock forming elements in non-polar hydrogen gas (Walther and Orville 1983). Combined with their size, this makes  $H_2$ -rich inclusions easily detectable even at temperatures  $> 1000\text{ }^\circ\text{C}$  (e.g. Figure 4c, e, f) and even in failed experiments, where water-containing inclusions show strong recrystallization features, such as negative crystal shapes or visible signs of fluid loss. Thus, a disappearance

of distinctive hydrogen inclusions is a very reliable optical marker of full miscibility between  $H_2O$  and  $H_2$ . The disappearance of pure water inclusions is less noticeable, as they commonly exhibit vapour bubbles that may be confused with a hydrogen-rich gas phase without Raman analysis.

Fluids trapped in the inclusions contained some silica and magnesium, from the dissolution of quartz and forsterite. As water is diluted by non-polar hydrogen molecules, the solubility of silica decreases dramatically (Walther and Orville

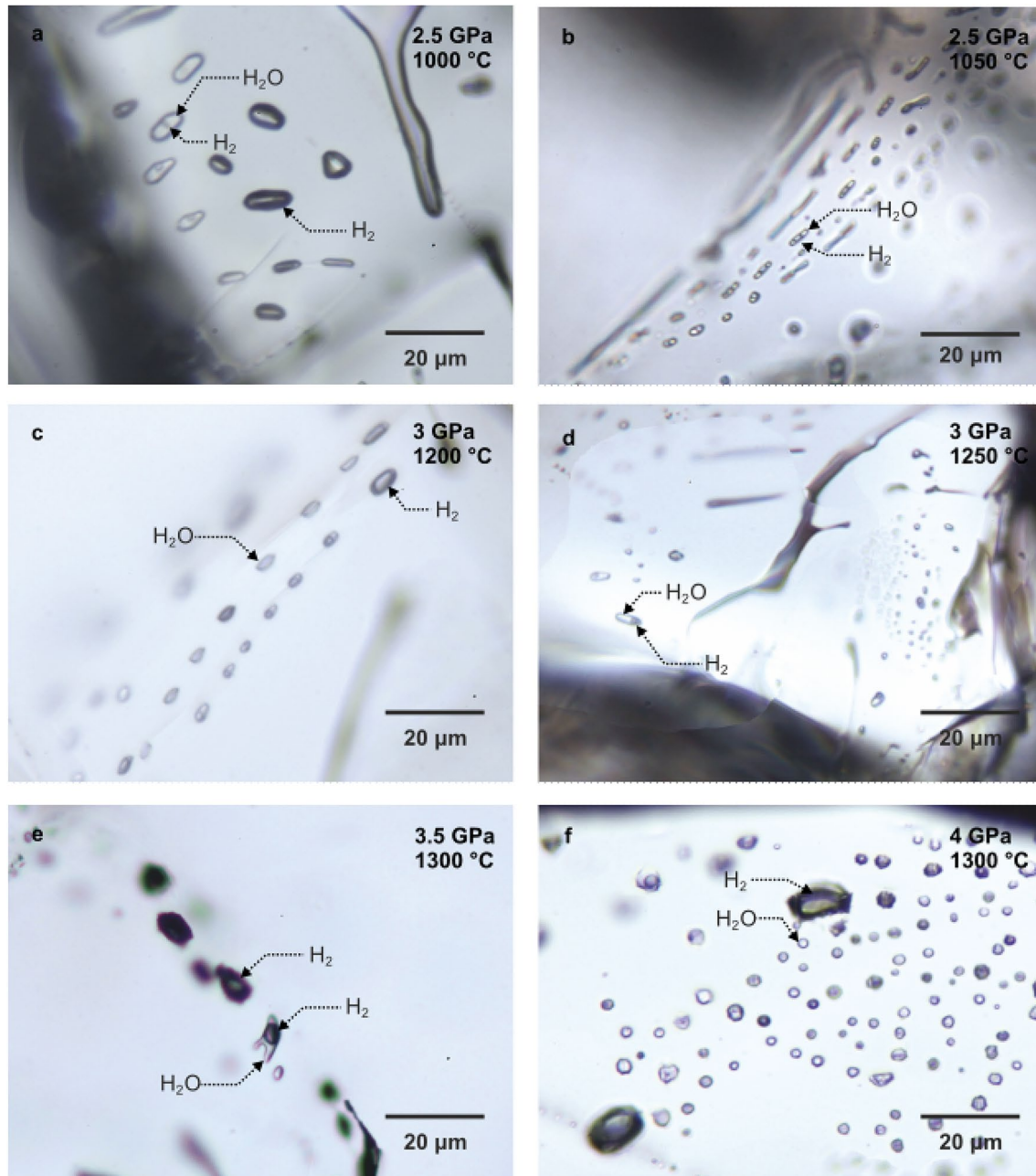


**Fig. 4** Synthetic fluid inclusions formed at 2.5–4 GPa in the immiscibility region, below the  $H_2$ - $H_2O$  critical curve **a, c, e, f** and above it in the miscibility region **b, d**. Images **c, d** and **f** are combinations of several separate photographs taken at different focal depths

1983). In laser-heated diamond cell experiments, the formation of  $\text{SiH}_4$  was observed as a result of the interaction of  $\text{H}_2$  and  $\text{SiO}_2$  (Shinozaki et al. 2014), however no detectable Raman signal of  $\text{SiH}_4$  was observed in our samples in the region of  $2180\text{--}2300\text{ cm}^{-1}$ . This suggests that this species either was not present in our experiments, or its concentration is negligible even in the low-density hydrogen-rich phase.

### Evidence for a reduced melting temperature of iron in the presence of $\text{H}_2$

In some of our experiments, we noted the occurrence of perfectly rounded droplets of metallic iron as inclusions in olivine crystals. This is consistent with the suggestion of Fukai et al. (2003) that alloying with  $\text{H}_2$  may strongly reduce the melting temperature of iron. As this observation is somewhat outside of the scope of this paper, the corresponding data are compiled in Figures S4 and S5 of the supplementary online material (file 2).

### $\text{H}_2\text{--H}_2\text{O}$ element partitioning experiments

Six experiments were performed (Table 2) in an attempt to investigate the partitioning of various elements between the coexisting  $\text{H}_2$ -rich and  $\text{H}_2\text{O}$ -rich fluid phases. Initially, elements capable of producing gaseous hydrides at our experimental conditions such as C, P, As, Se, and Te (Greenwood and Earnshaw 2012) were the primary targets of our investigation, as well as Xe, Cs, and Rb, which were planned to be used as internal standards. However, most of those experiments failed due to the reactivity of the selected chemical elements. Quantification of phosphorus in fluid inclusions in quartz (KVHP6) with the use of LA ICP-MS turned out to be impossible due to the incorporation of this element into newly-formed quartz, with the signal intensity from inclusion-free areas being comparable to the signal intensity from the inclusion itself. As, Se, and Te (KVHP7, KVHP8) were either completely lost to the inner platinum capsule, or they damaged the capsule during experiment

due to the formation of platinum compounds. However, the experiments with C, Xe, Rb, Cs and other elements present in the doped diopside glass (KVHP9, KVHP10, KVHP11) were successful. Experiments KVHP9 and KVHP10 were carried out at 2 GPa and  $750\text{ }^\circ\text{C}$ , less than  $100\text{ }^\circ\text{C}$  below the critical curve. Though the inclusions are relatively small, the immiscibility can still be easily observed. Samples from the KVHP9 (supplementary file 2, Figure S2) experiment were analysed with LA ICP-MS, but the small size of the inclusions ( $\sim 10\text{--}30\text{ }\mu\text{m}$ ) did not allow to detect a clear fractionation effect between the water and hydrogen-rich phases. Inclusions were also produced in the experiment KVHP11 at 2.3 GPa and  $675\text{ }^\circ\text{C}$  (supplementary file 2, Figure S3),  $\sim 275$  degrees below the critical curve. At those P–T conditions, inclusions were trapped deep in the immiscibility region to enhance any possible element partitioning. They range in size from  $10\text{ }\mu\text{m}$  to  $100\text{ }\mu\text{m}$  with multiple water and hydrogen inclusions of comparable size, while some inclusions with  $\text{H}_2$  are considerably larger (supplementary file 2, Figure S3b). Raman measurements of all types of inclusions and phases present in this sample yielded the first valuable result—hydrogen inclusions are rich in  $\text{CH}_4$  (supplementary file 2, Figure S3c, orange), while this species is almost absent from water inclusions. Only a minor  $\text{CH}_4$  signal can be seen in the vapour bubble of water-rich inclusions (supplementary file 2, Figure S3c, green and blue). Initially, carbon was added to the capsule in the form of  $\text{CaCO}_3$  as a minor impurity in the utilized  $\text{Ca}(\text{OH})_2$ . During the experiment in the Fe–FeO buffered capsule the presence of free hydrogen likely led to a rapid conversion of  $\text{CO}_3^{2-}$  to  $\text{CH}_4$ —a dominant carbon species at such conditions (C. Zhang and Duan 2009).

Further partitioning effects were unraveled with the use of LA ICP-MS with a typical inclusion laser ablation profile presented in Fig. 5 (full data available in supplementary file 1, Tables S1–S7). During ablation the gas phase is released first, hence the strongest xenon peak occurs at 32 s, followed by the remaining contents of the inclusion. As the fraction of gas phase in individual fluid inclusions increases (Fig. 6a) the Xe/Rb and Xe/Cs ratios tend to increase, demonstrating

**Table 2** Experiments investigating element partitioning associated with  $\text{H}_2\text{--H}_2\text{O}$  unmixing. In all experiments  $\text{H}_2$ ,  $\text{H}_2\text{O}$  and  $\text{H}_2 + \text{H}_2\text{O}$  inclusions were present. All runs were performed using natural quartz from Brazil and the double capsule technique

Experiment	Pressure, GPa	Temperature, $^\circ\text{C}$	Run duration, h	Starting materials
KVHP 6	2	750	22	$\text{Ca}(\text{OH})_2 + \text{CaCO}_3, \text{XeF}_2, \text{SiO}_2, \text{H}_2\text{O} + \text{RbCl} + \text{CsCl}, \text{Au}, \text{H}_3\text{PO}_4$
KVHP 7	2	750	22	$\text{Ca}(\text{OH})_2 + \text{CaCO}_3, \text{XeF}_2, \text{SiO}_2, \text{H}_2\text{O} + \text{RbCl} + \text{CsCl}, \text{Au}, \text{As}$
KVHP 8	2	750	22	$\text{Ca}(\text{OH})_2 + \text{CaCO}_3, \text{XeF}_2, \text{SiO}_2, \text{H}_2\text{O} + \text{RbCl} + \text{CsCl}, \text{Au}, \text{Se}, \text{Te}$
KVHP 9	2	750	22	$\text{Ca}(\text{OH})_2 + \text{CaCO}_3, \text{XeF}_2, \text{synthetic diopside-glass powder}, \text{H}_2\text{O} + \text{RbCl} + \text{CsCl}, \text{Au}$
KVHP 10	2	750	22	$\text{Ca}(\text{OH})_2 + \text{CaCO}_3, \text{XeF}_2, \text{synthetic diopside-glass powder}, \text{H}_2\text{O} + \text{RbCl} + \text{CsCl}, \text{Au}$
KVHP 11	2.3	675	18.5	$\text{Ca}(\text{OH})_2 + \text{CaCO}_3, \text{XeF}_2, \text{synthetic diopside-glass powder}, \text{H}_2\text{O} + \text{RbCl} + \text{CsCl}, \text{Au}$



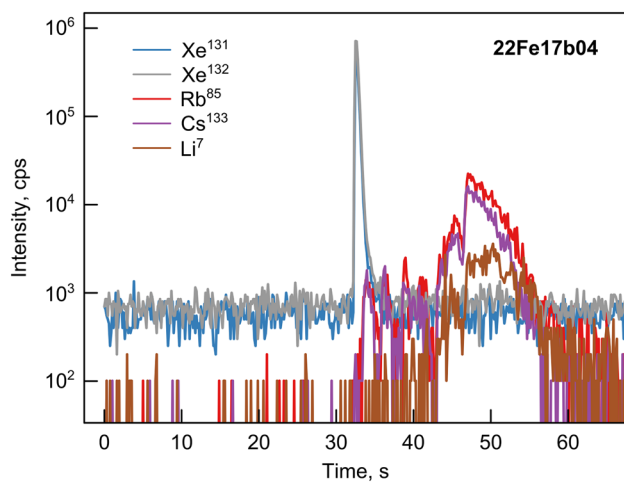


**Fig. 5** Laser ablation analysis of an individual gas-rich inclusion produced in the element partitioning experiment KVHP11

strong partitioning of alkali metals into the water phase. Xe, on the other hand, tends to partition into the gas phase. Although in similar-sized  $H_2$ -rich versus  $H_2O$ -rich fluid inclusions the intensities of the xenon signals are comparable (Fig. 6b), the lower density of the  $H_2$ -rich phase implies strong partitioning of Xe into the  $H_2$  phase. At 2.3 GPa and 675 °C, the density of pure water is 1.138 g/cm<sup>3</sup> (Wagner and Pruß 2002), and that of hydrogen 0.148 g/cm<sup>3</sup> (Leachman et al. 2009). Accordingly, if for  $H_2O$ -rich and  $H_2$ -rich inclusions of similar size the intensity of the xenon signal is about the same, then the concentration of Xe (i.e., the weight of Xe relative to that of the bulk fluid) is about 8 times higher in the  $H_2$ -rich phase, and Xe thus partitions by

definition by a factor of about 8 into that phase (supplementary file 1, Table S1). The density of  $CH_4$ , that is abundant in gas inclusions, at given experimental conditions is 0.58 g/cm<sup>3</sup> (Jiang et al. 2022) which possibly reduces the partitioning coefficient, yet not by much since even pure methane is half as dense as water. The other trace elements measured, including the rare earths, alkalis, alkaline earths and various high-field strength elements, appear to partition strongly into the  $H_2O$ -rich phase.

## Discussion

### Comparison with previous data

The experimental method used in the current study to establish the position of the  $H_2$ - $H_2O$  critical curve is very similar to the one of Bali et al. (2013). The only significant difference is the shorter run durations at temperatures above 850 °C (Table 1). As may be seen from Fig. 2, the experimental data are extremely similar in the pressure range where the two studies overlap, with both critical curves having the same slope. The only significant deviation between the two datasets that cannot be explained by thermocouple uncertainty or temperature gradients in the piston-cylinder assembly is a single experiment of Bali et al. at 2.3 GPa and 900 °C, showing immiscibility where our data suggests that fluids are still miscible. Yet in their work the critical curve was drawn not below this experimental point, but across it, which indicates that it may have been a borderline case located extremely close to the curve, where distinguishing between immiscibility or miscibility patterns is

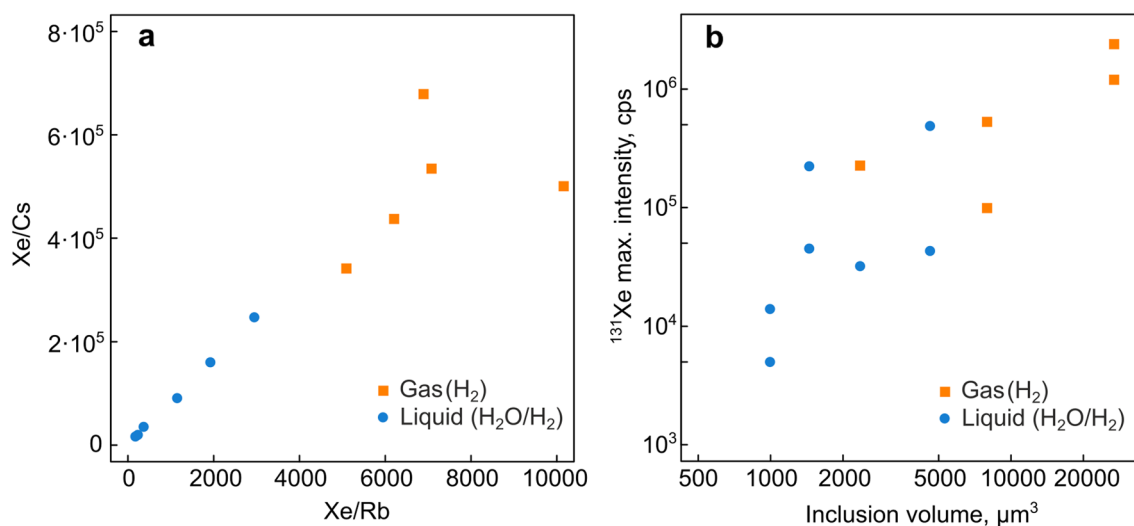


**Fig. 6** **a** LA-ICP-MS-established Xe/Cs count ratios plotted versus Xe/Rb count ratios for individual inclusions, and **b** <sup>131</sup>Xe signal intensities plotted versus inclusion volume. Data for hydrogen-rich inclu-

sions are shown in orange, whereas data for inclusions with liquid water and possible co-trapped hydrogen are shown in blue

not straightforward. Additionally, the critical curve of Bali et al. exhibits a gradual change in slope as quartz is replaced by forsterite as host crystal. This effect was not well manifested in our data with the slope being in fact almost linear and continuous from 1.5 to 2.5 GPa in the range where the host crystal changed. Potentially such effects could result from hydrogen diffusion, affecting the inclusion composition and data interpretation. Hydrogen diffusion has been known to be quite rapid in quartz with significant shift in phase assemblage occurring at 700 °C in experiments lasting for 7 days (Mavrogenes and Bodnar, 1993). Yet this process is unlikely to be relevant for our experiments, since the inclusions are in equilibrium with the fluid during the run, while decompression and sample processing times have been minimized. Even though some minor hydrogen loss is possible, the Raman detection limit for H<sub>2</sub> is as low as 1–3 bar (Mavrogenes and Bodnar 1994). This suggests that even in case of partial loss the inclusion type would be determined correctly.

Both in the experiments of Bali et al. (2013) and in those of the present study, fluid composition was controlled by an external Fe-FeO-H<sub>2</sub>O buffer. This buffer will produce H<sub>2</sub> by the reaction  $\text{Fe} + \text{H}_2\text{O} = \text{FeO} + \text{H}_2$ ; the H<sub>2</sub> will diffuse into the inner capsule until the equilibrium H<sub>2</sub>/H<sub>2</sub>O ratio in the charge is reached. According to the observations from synthetic fluid inclusions in the range of full miscibility (e.g. Figure 4b), this fluid contains H<sub>2</sub> and H<sub>2</sub>O in a molar ratio close to unity, consistent with thermodynamic predictions. However, due to the experimental setup, the H<sub>2</sub>/H<sub>2</sub>O ratio cannot be independently varied in these runs. It is therefore not impossible that for a somewhat different H<sub>2</sub>/H<sub>2</sub>O ratio, the miscibility gap could close at a somewhat higher temperature. Our experimental observations suggest, however, that this is unlikely to be a significant effect. The fluid inclusions (e.g. Figure 4c) show that at temperatures not far below our critical curve, nearly pure H<sub>2</sub> coexists with nearly pure H<sub>2</sub>O. This implies that the temperature of complete miscibility is rather insensitive to the actual H<sub>2</sub>/H<sub>2</sub>O ratio.

The results of Seward and Franck (1981), who measured immiscibility in systems with variable H<sub>2</sub>-H<sub>2</sub>O fractions to 440 °C and 250 MPa, are located outside of our experimental range and just slightly below the extrapolation of our critical curve. Though the discrepancy between this extrapolation and Seward and Franck's data is minor, the explanation for it is straightforward. Our 600 °C and 1 GPa experiment is probably located almost exactly on the critical curve itself, as the pure hydrogen inclusions in this run are small and comparatively rare. Thus, at 1 GPa the real slope may be slightly steeper than we assumed. The extrapolation would then almost perfectly align with the critical curve of Seward and Franck (1981).

A direct comparison of our experiments with the computational results of Bergermann et al. (2021), which support

the existence of immiscibility between water and hydrogen, or with those of Soubiran and Militzer (2015), which suggest the absence of such an effect, is complicated. Due to the sensitivity of the simulations to the choice of the cutoff radius value and the imperfections of analytical two-body interaction potentials, the disagreement of existing computational studies with our experimental data is quite significant. The results of Bergermann et al. (2021) indicate that at temperatures above 1100 °C, the experimental critical curve approaches the simulated curve and intersects it at ~1350 °C. With no miscibility observed in our experiments above 3 GPa the experimental data for 3.5 and 4 GPa is in seeming agreement with the simulated critical curve, however the general difference in slopes of the two curves suggests that this agreement is partially coincidental.

### H<sub>2</sub>-H<sub>2</sub>O immiscibility in Earth's interior and the formation of super-reduced mineral assemblages

Several mechanisms for the formation of super-reduced mineral associations have been proposed in the past. A first hypothesis suggested a deep origin (e.g. R. Zhang et al. 2016), assuming that phases such as moissanite, native silicon, iron, nitrides and phosphides crystallized at depths exceeding 200 km, where oxygen fugacity is expected to be low, although by far not low enough to stabilize SiC (Frost and McCammon 2008). For example, the SiC grains coexisting with diamond, native Fe and FeO from the Luobusa ophiolites (Tibet) were assumed to have formed at pressures of 8.5–9 GPa (R. Zhang et al. 2016), corresponding to a depth of ~300 km.

A second hypothesis, described in detail by Bali et al. (2013), proposes that oxygen fugacities at the level of the IW buffer and below do not necessarily require deep mantle conditions. The authors suggest that low fugacities can be achieved locally, via gradual water removal from immiscible H<sub>2</sub>-H<sub>2</sub>O fluids even at relatively shallow conditions in the upper mantle. At first, reducing fluids may form at 150–200 km depth (Fig. 7a, b) via slab dehydration (Kawamoto 2018). As water and hydrogen fluids percolate through the mantle, water is being sequestered in hydrous melts (Ni et al. 2011; Shen and Keppler 1995), incorporated into nominally anhydrous minerals (Fei and Katsura 2020; Hirschmann et al. 2005; Mierdel et al. 2007) or hydrous phases (Smyth 2018). As the amount of available H<sub>2</sub>O in the system decreases, the oxygen fugacity decreases as well (Bali et al. 2013) making the formation of super reducing phases plausible. Golubkova et al. (2016) suggested a similar model of H<sub>2</sub>O removal from reducing fluids as a mechanism for attaining ultra-reducing conditions in the shallow mantle, although without explicitly referring to H<sub>2</sub>-H<sub>2</sub>O immiscibility.

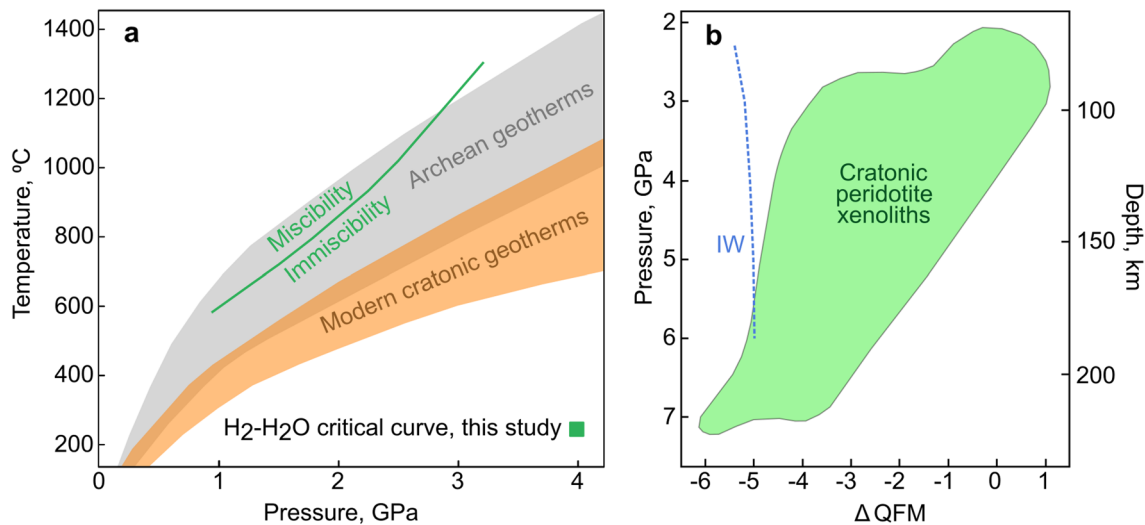


**Fig. 7** **a** Archean (grey) (Mareschal and Jaupart 2006) and modern (orange) geotherms (Hasterok and Chapman 2011; Rudnick and Nyblade 1999), compared with the H<sub>2</sub>-H<sub>2</sub>O immiscibility curve. **b** Oxygen fugacity range of cratonic peridotites based on xenolith data (Creighton et al. 2009; Goncharov et al. 2012; Lazarov et al. 2009;

McCammon and Kopylova 2004; ; Woodland and Koch 2003; Yaxley et al. 2012). The dashed blue line shows IW buffer conditions (Campbell et al. 2009) calculated along the hot Kalahari geotherm (Rudnick and Nyblade 1999), which is shown in **a** as the upper bound of the modern cratonic geotherms

Carbon-rich phases—graphite, diamond, or hydrocarbons—are extremely important parts of reduced environments in the upper mantle (Frost and McCammon 2008). Although a detailed investigation of carbon geochemistry in the presence of H<sub>2</sub>-H<sub>2</sub>O fluids at IW buffer conditions is beyond the scope of our study, we did observe significant methane generation from minor carbonate impurities (<0.5 wt. %) in the capsule. Existing experiments investigating immiscibility in the C-H-O system (Li 2016) are in full agreement with our experiments and indicate that the presence of carbon at least does not move the critical curve to lower temperatures at pressures below 3 GPa. In general, if methane is available at upper mantle conditions, diamond may form during the evolution of such fluids in the lithospheric mantle (e.g. Matjuschkin et al. 2019; Thomassot et al. 2007). Additionally, metastable low-pressure, low-temperature diamonds have been found to form in CH<sub>4</sub>-rich fluid inclusions during the serpentinization of oceanic lithosphere (Pujol-Solà et al. 2020). However, it is currently unknown how widespread this process is. In general, metasomatic processes caused by CH<sub>4</sub>-H<sub>2</sub>-rich fluids have been well documented (Vitale Brovarone et al. 2017) in ophicarbonates from the Italian Alps with abundant graphite and fluid inclusions being present in the rocks. Observations from our element partitioning experiments suggest that within the H<sub>2</sub>-H<sub>2</sub>O immiscibility field, methane partitions into the highly mobile H<sub>2</sub>-rich fluid phase that in turn may be a precursor for the formation of diamonds, graphite, or moissanite.

Native iron, nickel, iron silicide, platinum and other metals and alloys have been described in metal-enriched

xenoliths from Avacha volcano that brought up samples from the mantle wedge below the Kamchatka peninsula (Ishimaru et al. 2009; Kepezhinskias et al. 2022). Formation conditions for this suite of rocks and associated metals are estimated as 792–1100 °C and 1–3 GPa (Kepezhinskias et al. 2022 and references within), consistent with the origin in a supra-subduction zone environment at rather shallow depth in the mantle, and can occur via the mechanism proposed by Bali et al. (2013) and in our study. In summary, our data suggest that super-reduced phases are not necessarily associated with UHP or UHT conditions, but can form at ~100–150 km or even shallower levels in the upper mantle through reactions involving reducing immiscible H<sub>2</sub>-CH<sub>4</sub> fluids.

### H<sub>2</sub>-H<sub>2</sub>O unmixing as a possible cause for mantle oxidation and the early loss of Earth's noble gases

Isotopes of noble gases, especially of xenon and neon, have traditionally been used to constrain Earth's early outgassing and atmosphere composition (e.g. Allègre et al. 1987; Marty 1989). The first atmospheres of Earth, Mars and Venus supposedly formed as the result of rapid gas release from the planetary interior, or by equilibration with a magma ocean, occurring shortly after core formation (Gaillard et al. 2022; Lammer et al. 2018; Tieloff et al. 2000). During those times the Earth's upper mantle, according to the model of Rubie et al. (2011), was hotter than in the Archaean (Fig. 7a) and was extremely reduced. However, this state lasted only for a short time: Cerium concentrations in the oldest surviving zircons suggest rapid upper mantle oxidation (Smythe and

Brenan 2016; Trail et al. 2011) that was completed 200 Myr after planetary formation, though the atmosphere itself may have remained reducing for a longer time (e.g. Kasting et al. 1993; Holland 2002).

Bali et al. (2013) suggested that rapid upper mantle oxidation was caused by the appearance of a miscibility gap between water and hydrogen when the planet cooled down. As noted by Sharp et al. (2013), rapid hydrogen degassing may also explain differences in water content and isotope compositions (H, Cl) in the Earth-Moon system. Hydrogen is easily transferred to the fluid phase during degassing of silicate melts (Hirschmann et al. 2012; Moore et al. 1998), thus the emergence of immiscibility between H<sub>2</sub> and H<sub>2</sub>O may trigger the formation of a buoyant and low-viscosity H<sub>2</sub>-dominant phase, followed by its rapid upward percolation (Bali et al. 2013; Sharp et al. 2013). Such a scenario is plausible if geotherms crossed the immiscibility curve, intensifying hydrogen phase loss rate and driving the upper mantle oxygen fugacity to higher values. Our new data show a steep increase of the critical curve at pressures above 2 GPa (Fig. 7a). This suggests that even for very hot geotherms in the early Archean or late Hadean, H<sub>2</sub>-H<sub>2</sub>O immiscibility occurred in the deeper parts of the upper mantle. Therefore, the scenario of early mantle oxidation by selective loss of a highly buoyant H<sub>2</sub>-rich fluid phase is very plausible.

Noble gas isotope data supports this idea, suggesting increased outgassing flux during the first 20–30 Myr after core formation (Kunz et al. 1998). One of the anomalies observed in the Earth's upper mantle noble gas compositions is the relative underabundance of <sup>129</sup>Xe, produced via the decay of <sup>129</sup>I (t<sub>1/2</sub> = 1.6 × 10<sup>7</sup> yr) that went extinct ~ 100 Myr after the formation of the solar system (Mukhopadhyay 2012). Similarly, there is a striking deficiency of xenon isotopes produced by spontaneous fission of now-extinct Pu (Kunz et al. 1998). Xenon is the least soluble in silicate melts of all noble gases (Schmidt and Keppler 2002; Shibata et al. 1998) and thus one would expect it to preferentially partition into a fluid phase. As can be seen from our partitioning experiments, xenon enters preferentially the reduced H<sub>2</sub>-rich phase. Thus, the early and rapid decrease in radiogenic xenon isotopes in the mantle can be explained by its partitioning into a hydrogen-rich phase during unmixing, subsequent degassing and then loss from the Earth's atmosphere for example by impact erosion during the late veneer event (Kruijer et al. 2015; Walker 2009).

Based on existing thermal evolution models (Herzberg et al. 2010; Korenaga 2006; Rubie et al. 2011) and degassing constraints (Kunz et al. 1998; Mukhopadhyay 2012), we estimate that H<sub>2</sub>-H<sub>2</sub>O unmixing may have occurred ~ 50–150 Myr after planetary formation, which is consistent with the evidences for an oxidized upper mantle 4350 Myr before present (Smythe and Brenan 2016; Trail et al. 2011). H<sub>2</sub> degassing may not be exclusive to Earth but may have

occurred on Mars and Venus as well. This makes rapid early hydrogen escape, related to H<sub>2</sub>-H<sub>2</sub>O immiscibility, a possible common feature of the evolution of rocky planets, with the underabundance of radiogenic <sup>129</sup>Xe being a prominent marker of this process.

## Conclusions

1. The strong increase in the critical curve of the H<sub>2</sub>-H<sub>2</sub>O system observed above 2 GPa in this study implies that immiscibility between H<sub>2</sub> and H<sub>2</sub>O may have occurred in the deeper parts of the upper mantle already very early in Earth's history, when ambient mantle temperatures were much higher than today.
2. We present the first experimental evidence that Xe—and by inference also other noble gases—strongly partitions into the H<sub>2</sub>-rich gas phase.
3. Degassing of a H<sub>2</sub>-rich fluid from the mantle is a plausible mechanism for both the early oxidation of the mantle and for the selective loss of noble gases in the Hadean.
4. In the modern Earth, the local occurrence of immiscible H<sub>2</sub>-rich fluids may be responsible for the formation of ultra-reduced mantle domains containing moissanite. These domains may form already at rather shallow depth in the mantle.

**Supplementary Information** The online version contains supplementary material available at <https://doi.org/10.1007/s00410-023-02019-7>.

**Acknowledgements** We would like to thank Detlef Krauß for SEM & WDS analyses, Raphael Njul and Alexander Rother for sample preparation and polishing, as well as Greta Rustioni for providing the glass sample MORB2-2D2. This study was partially supported by Deutsche Forschungsgemeinschaft through the international research Training Network “Deep Earth Volatile Cycles” GRK 2156/1. Constructive reviews by Dimitri Sverjensky and by two anonymous referees helped to improve the manuscript.

**Funding** Open Access funding enabled and organized by Projekt DEAL.

**Data availability** All of the data supporting the findings of this study are included within the paper itself and its supplementary files.

**Open Access** This article is licensed under a Creative Commons Attribution 4.0 International License, which permits use, sharing, adaptation, distribution and reproduction in any medium or format, as long as you give appropriate credit to the original author(s) and the source, provide a link to the Creative Commons licence, and indicate if changes were made. The images or other third party material in this article are included in the article's Creative Commons licence, unless indicated otherwise in a credit line to the material. If material is not included in the article's Creative Commons licence and your intended use is not permitted by statutory regulation or exceeds the permitted use, you will need to obtain permission directly from the copyright holder. To view a copy of this licence, visit <http://creativecommons.org/licenses/by/4.0/>.



## References

- Abbott D, Burgess L, Longhi J, Smith WHF (1994) An empirical thermal history of the Earth's upper mantle. *J Geophys Res* 99(B7):13835–13850. <https://doi.org/10.1029/94jb00112>
- Allègre CJ, Staudacher T, Sarda P (1987) Rare gas systematics: formation of the atmosphere, evolution and structure of the Earth's mantle. *Earth Planet Sci Lett* 81(2–3):127–150. [https://doi.org/10.1016/0012-821X\(87\)90151-8](https://doi.org/10.1016/0012-821X(87)90151-8)
- Armstrong K, Frost D, McCammon C, Rubie D, Ballaran T (2019) Deep magma ocean formation set the oxidation state of Earth's mantle. *Science* 365(6456):903–906. <https://doi.org/10.1126/science.aax8376>
- Bali E, Audétat A, Keppler H (2013) Water and hydrogen are immiscible in Earth's mantle. *Nature* 495(7440):220–222. <https://doi.org/10.1038/nature11908>
- Ballhaus C (1993) Redox states of lithospheric and asthenospheric upper mantle. *Contrib to Mineral Petrol* 114(3):331–348. <https://doi.org/10.1007/BF01046536>
- Bergemann A, French M, Redmer R (2021) Gibbs-ensemble monte carlo simulation of H<sub>2</sub>–H<sub>2</sub>O mixtures. *Phys Chem Chem Phys* 23(22):12637–12643. <https://doi.org/10.1039/d1cp00515d>
- Bose K, Ganguly J (1995) Quartz-coesite transition revisited: reversed experimental determination at 500–1200 °C and retrieved thermochemical properties. *Am Mineral* 80(3–4):231–238. <https://doi.org/10.2138/am-1995-3-404>
- Campbell A, Danielson L, Righter K, Seagle CT, Wang Y, Prakapenka V (2009) High pressure effects on the iron-iron oxide and nickel-nickel oxide oxygen fugacity buffers. *Earth Planet Sci Lett* 286(3–4):556–564. <https://doi.org/10.1016/j.epsl.2009.07.022>
- Chou I (1987) Oxygen buffer and hydrogen sensor techniques at elevated pressures and temperatures. In: Ulmer G, Barnes H (eds) *Hydrothermal Experimental Techniques*. John Wiley, New York, pp 61–99
- Creighton S, Stachel T, Matveev S, Höfer H, McCammon C, Luth RW (2009) Oxidation of the kaapvaal lithospheric mantle driven by metasomatism. *Contrib to Min Petrol* 157(4):491–504. <https://doi.org/10.1007/s00410-008-0348-3>
- Dobrzhinetskaya L, Mukhin P, Wang Q, Wirth R, O'Bannon E, Zhao W, Eppelbaum L, Sokhonchuk T (2018) Moissanite (SiC) with metal-silicide and silicon inclusions from tuff of Israel: Raman spectroscopy and electron microscope studies. *Lithos* 310–311:355–368. <https://doi.org/10.1016/j.lithos.2017.04.001>
- Fei H, Katsura T (2020) Pressure dependence of proton incorporation and water solubility in olivine. *J Geophys Res Solid Earth* 125(2):018813. <https://doi.org/10.1029/2019JB018813>
- Frost D, McCammon C (2008) The redox state of Earth's mantle. *Annu Rev Earth Planet Sci* 36(1):389–420. <https://doi.org/10.1146/annurev.earth.36.031207.124322>
- Fukai Y, Mori K, Shinomiya H (2003) The phase diagram and superabundant vacancy formation in Fe-H alloys under high hydrogen pressures. *J Alloys Compd* 348(1–2):105–109. [https://doi.org/10.1016/S0925-8388\(02\)00806-X](https://doi.org/10.1016/S0925-8388(02)00806-X)
- Gaillard F, Bernadou F, Roskosz M, Bouhifd MA, Marrocchi Y, Iacono-Marziano G, Moreira M, Scaillet B, Rogerie G (2022) Redox controls during magma ocean degassing. *Earth Planet Sci Lett* 577:117255
- Golubkova A, Schmidt M, Connolly JAD (2016) Ultra-reducing conditions in average mantle peridotites and in podiform chromitites: a thermodynamic model for moissanite (SiC) formation. *Contrib to Min Petrol* 171(5):1–17
- Goncharov A, Ionov D, Doucet L, Pokhilenko L (2012) Thermal state, oxygen fugacity and C-O-H fluid speciation in cratonic lithospheric mantle: New data on peridotite xenoliths from the Udachnaya kimberlite, Siberia. *Earth Planet Sci Lett* 357–358:99–110. <https://doi.org/10.1016/j.epsl.2012.09.016>
- Greenwood N, Earnshaw A (2012) *Chemistry of the Elements*. Elsevier, Oxford
- Hasterok D, Chapman D (2011) Heat production and geotherms for the continental lithosphere. *Earth Planet Sci Lett* 307(1–2):59–70. <https://doi.org/10.1016/j.epsl.2011.04.034>
- Herzberg C, Condie K, Korenaga J (2010) Thermal history of the Earth and its petrological expression. *Earth Planet Sci Lett* 292(1–2):79–88. <https://doi.org/10.1016/j.epsl.2010.01.022>
- Hirschmann M, Aubaud C, Withers A (2005) Storage capacity of H<sub>2</sub>O in nominally anhydrous minerals in the upper mantle. *Earth Planet Sci Lett* 236(1–2):167–181. <https://doi.org/10.1016/j.epsl.2005.04.022>
- Hirschmann M, Withers A, Ardia P, Foley N (2012) Solubility of molecular hydrogen in silicate melts and consequences for volatile evolution of terrestrial planets. *Earth Planet Sci Lett* 345–348:38–48. <https://doi.org/10.1016/j.epsl.2012.06.031>
- Holland H (2002) Volcanic gases, black smokers, and the great oxidation event. *Geochim Cosmochim Acta* 66(21):3811–3826. [https://doi.org/10.1016/S0016-7037\(02\)00950-X](https://doi.org/10.1016/S0016-7037(02)00950-X)
- Ishimaru S, Arai S, Shukuno H (2009) Metal-saturated peridotite in the mantle wedge inferred from metal-bearing peridotite xenoliths from Avacha volcano. *Kamchatka Earth Planet Sci Lett* 284(3–4):352–360. <https://doi.org/10.1016/j.epsl.2009.04.042>
- Jiang S, Guo T, Yu Y, Hu J (2022) Molecular dynamics simulation and a cubic equation of state of supercritical methane Up to 3000 K and 3000 MPa. *Int J Thermophys* 43:22. <https://doi.org/10.1007/s10765-021-02952-4>
- Kaminsky F (2012) Mineralogy of the lower mantle: a review of “super-deep” mineral inclusions in diamond. *Earth Sci Rev* 110(1–4):127–147. <https://doi.org/10.1016/j.earscirev.2011.10.005>
- Kasting J, Egger D, Raeburn S (1993) Mantle redox evolution and the oxidation state of the Archean atmosphere. *J Geol* 101(2):245–257. <https://doi.org/10.1086/648219>
- Kawamoto T (2018) Hydrous phases and water transport in the subducting slab. *Rev Mineral Geochem* 62:273–290. <https://doi.org/10.2138/rmg.2006.62.12>
- Kepezhinskas P, Berdnikov N, Kepezhinskas N, Konovalova N (2022) Metals in Avachinsky peridotite xenoliths with implications for redox heterogeneity and metal enrichment in the Kamchatka mantle wedge. *Lithos* 412:106610. <https://doi.org/10.1016/j.lithos.2022.106610>
- Korenaga J (2006) Archean geodynamics and the thermal evolution of Earth. *Geophys Monogr Ser* 164:7. <https://doi.org/10.1029/164GM03>
- Kruijer T, Kleine T, Fischer-Gödde M, Sprung P (2015) Lunar tungsten isotopic evidence for the late veneer. *Nature* 520(7548):534–537. <https://doi.org/10.1038/nature14360>
- Kunz J, Staudacher T, Allègre CJ (1998) Plutonium-fission xenon found in Earth's mantle. *Science* 280(5365):877–880. <https://doi.org/10.1126/science.280.5365.877>
- Lammer H, Zerkle AL, Gebauer S, Tosi N, Noack L, Scherf M, Pilat-Lohinger E, Güdel M, Grenfell JL, Godolt M, Nikolaou A (2018) Origin and evolution of the atmospheres of early Venus, Earth and Mars. *Astron Astrophys Rev* 26(1):1–72. <https://doi.org/10.1007/s00159-018-0108-y>
- Lathe C, Koch-Müller M, Wirth R, van Westrenen W, Mueller H, Schilling F, Lauterjung J (2005) The influence of OH in coesite on the kinetics of the coesite-quartz phase transition. *Am Miner* 90(1):36–43. <https://doi.org/10.2138/am.2005.1662>
- Lazarov M, Woodland A, Brey G (2009) Thermal state and redox conditions of the Kaapvaal mantle: A study of xenoliths from the Finsch mine, South Africa. *Lithos* 112:913–923. <https://doi.org/10.1016/j.lithos.2009.03.035>



- Leachman J, Jacobsen R, Penoncello S, Lemmon E (2009) Fundamental equations of state for parahydrogen, normal hydrogen, and orthohydrogen. *J Phys Chem Ref Data* 38(3):721–748. <https://doi.org/10.1063/1.3160306>
- Li Y (2016) Immiscible C-H-O fluids formed at subduction zone conditions. *Geochem Perspect Lett*. <https://doi.org/10.7185/geochemlet.1702>
- Mareschal J, Jaupart C (2006) Archean geodynamics and environments. *Geophys Monogr Ser* 164:61–73
- Marty B (1989) Neon and xenon isotopes in MORB: implications for the earth-atmosphere evolution. *Earth Planet Sci Lett* 94(1–2):45–56. [https://doi.org/10.1016/0012-821X\(89\)90082-4](https://doi.org/10.1016/0012-821X(89)90082-4)
- Matjuschkin V, Woodland A, Yaxley G (2019) Methane-bearing fluids in the upper mantle: an experimental approach. *Contrib to Mineral Petrol* 174(1):1–14. <https://doi.org/10.1007/s00410-018-1536-4>
- Mavrogenes J, Bodnar R (1994) Hydrogen movement into and out of fluid inclusions in quartz: Experimental evidence and geologic implications. *Geochim Cosmochim Acta* 58(1):141–148. [https://doi.org/10.1016/0016-7037\(94\)90452-9](https://doi.org/10.1016/0016-7037(94)90452-9)
- McCammon C, Kopylova M (2004) A redox profile of the slave mantle and oxygen fugacity control in the cratonic mantle. *Contrib to Mineral Petrol* 148(1):55–68. <https://doi.org/10.1007/s00410-004-0583-1>
- Mierdel K, Keppler H, Smyth J, Langenhorst F (2007) Water solubility in aluminous orthopyroxene and the origin of Earth's asthenosphere. *Science* 315(5810):364–368. <https://doi.org/10.1126/science.1135422>
- Moore G, Vennemann T, Carmichael I (1998) An empirical model for the solubility of H<sub>2</sub>O in magmas to 3 kilobars. *Am Mineral* 83(1–2):36–42. <https://doi.org/10.2138/am-1998-1-203>
- Mukhopadhyay S (2012) Early differentiation and volatile accretion recorded in deep-mantle neon and xenon. *Nature* 486(7401):101–104. <https://doi.org/10.1038/nature11141>
- Nazzareni S, Nestola F, Zanon V, Bindi L, Scricciolo E, Petrelli M, Zanatta M, Mariotto G, Giuli G (2019) Discovery of moissanite in a peralkaline syenite from the Azores Islands. *Lithos* 324–325:68–73. <https://doi.org/10.1016/j.lithos.2018.10.036>
- Ni H, Keppler H, Behrens H (2011) Electrical conductivity of hydrous basaltic melts: implications for partial melting in the upper mantle. *Contrib to Mineral Petrol* 162(3):637–650. <https://doi.org/10.1007/s00410-011-0617-4>
- Pitzer K, Sterner S (1994) Equations of state valid continuously from zero to extreme pressures for H<sub>2</sub>O and CO<sub>2</sub>. *J Chem Phys* 101(4):3111–3116. <https://doi.org/10.1063/1.467624>
- Pujol-Solà N, Proenza JA, Garcia-Casco A, González-Jiménez JM, Andreazini A, Melgarejo JC, Gervilla F (2018) An alternative scenario on the origin of ultra-high pressure (UHP) and super-reduced (SuR) minerals in ophiolitic chromitites: A case study from the Mercedita deposit (Eastern Cuba). *Minerals* 8(10):433. <https://doi.org/10.3390/min8100433>
- Pujol-Solà N, Garcia-Casco A, Proenza JA, González-Jiménez JM, del Campo A, Colás V, Canalis A, Sánchez-Navas A, Roqué-Rosell J (2020) Diamond forms during low pressure serpentinisation of oceanic lithosphere. *Geochem Perspect Lett* 15:19–24. <https://doi.org/10.7185/geochemlet.2029>
- Rubie D, Frost D, Mann U, Asahara Y, Nimmo F, Tsuno K, Kegler P, Holzheid A, Palme H (2011) Heterogeneous accretion, composition and core-mantle differentiation of the Earth. *Earth Planet Sci Lett* 301(1–2):31–42. <https://doi.org/10.1016/j.epsl.2010.11.030>
- Rudnick R, Nyblade A (1999) The thickness and heat production of archaic lithosphere: constraints from xenolith thermobarometry and surface heat flow. *mantle petrology: field observations and high pressure experimentation: a tribute to francis R. Boyd*. 6:3–12
- Rustioni G, Audétat A, Keppler H (2019) Experimental evidence for fluid-induced melting in subduction zones. *Geochem Perspect Lett* 11:49–54. <https://doi.org/10.7185/geochemlet.1925>
- Schmidt B, Keppler H (2002) Experimental evidence for high noble gas solubilities in silicate melts under mantle pressures. *Earth Planet Sci Lett* 195(3–4):277–290. [https://doi.org/10.1016/S0012-821X\(01\)00584-2](https://doi.org/10.1016/S0012-821X(01)00584-2)
- Seward T, Franck E (1981) System hydrogen water up to 440 °C and 2500 bar pressure. *Ber Bunsenges Phys Chem* 85(1):2–7. <https://doi.org/10.1002/bbpc.1981085010>
- Sharp Z, McCubbin F, Shearer C (2013) A hydrogen-based oxidation mechanism relevant to planetary formation. *Earth Planet Sci Lett* 380:88–97. <https://doi.org/10.1016/j.epsl.2013.08.015>
- Shen A, Keppler H (1995) Infrared spectroscopy of hydrous silicate melts to 1000°C and 10 kbar: direct observation of H<sub>2</sub>O speciation in a diamond-anvil cell. *Am Mineral* 80(11–12):1335–1338. <https://doi.org/10.2138/am-1995-11-1223>
- Shibata T, Takahashi E, Matsuda J (1998) Solubility of neon, argon, krypton, and xenon in binary and ternary silicate systems: a new view on noble gas solubility. *Geochim Cosmochim Acta* 62(7):1241–1253. [https://doi.org/10.1016/S0016-7037\(98\)00046-5](https://doi.org/10.1016/S0016-7037(98)00046-5)
- Shinozaki A, Kagi H, Noguchi N, Hirai H, Ohfuji H, Okada T, Nakano S, Yagi T (2014) Formation of SiH<sub>4</sub> and H<sub>2</sub>O by the dissolution of quartz in H<sub>2</sub> fluid under high pressure and temperature. *Am Mineral* 99(7):1265–1269. <https://doi.org/10.2138/am.2014.4798>
- Shiryaev A, Griffin W, Stoyanov E (2011) Moissanite (SiC) from kimberlites: Polytypes, trace elements, inclusions and speculations on origin. *Lithos* 122(3–4):152–164. <https://doi.org/10.1016/j.lithos.2010.12.011>
- Smyth J (2018) Hydrogen in high pressure silicate and oxide mineral structures. *Rev Mineral Geochem* 62(1):85–115. <https://doi.org/10.2138/rmg.2006.62.5>
- Smythe D, Brennan J (2016) Magmatic oxygen fugacity estimated using zircon-melt partitioning of cerium. *Earth Planet Sci Lett* 453:260–266. <https://doi.org/10.1016/j.epsl.2016.08.013>
- Soubiran F, Militzer B (2015) Miscibility calculations for water and hydrogen in giant planets. *Astrophys J* 806(2):228. <https://doi.org/10.1088/0004-637X/806/2/228>
- Thomassot E, Cartigny P, Harris J (2007) Methane-related diamond crystallization in the Earth's mantle: Stable isotope evidences from a single diamond-bearing xenolith. *Earth Planet Sci Lett* 257(3–4):362–371. <https://doi.org/10.1016/j.epsl.2007.02.020>
- Tingle T, Roedder E, Green H (1992) Formation of fluid inclusions and etch tunnels in olivine at high pressure. *Am Mineral* 77(3–4):296–302
- Trail D, Watson E, Tailby N (2011) The oxidation state of Hadean magmas and implications for early Earth's atmosphere. *Nature* 480(7375):79–82. <https://doi.org/10.1038/nature10655>
- Trieloff M, Kunz J, Clague D, Harrison D, Allègre C (2000) The nature of pristine noble gases in mantle plumes. *Science* 288(5468):1036–1038. <https://doi.org/10.1126/science.288.5468.1036>
- Trumbull R, Yang J-S, Robinson P, Di Pierro S, Vennemann T, Wiedenbeck M (2009) The carbon isotope composition of natural SiC (moissanite) from the Earth's mantle: New discoveries from ophiolites. *Lithos* 113(3–4):612–620. <https://doi.org/10.1016/j.lithos.2009.06.033>
- Tuff J, Wade J, Wood B (2013) Volcanism on Mars controlled by early oxidation of the upper mantle. *Nature* 498(7454):342–345. <https://doi.org/10.1038/nature12225>
- Ulmer G, Grandstaff D, Woermann E, Göbbels M, Schönitz M, Woodland A (1998) The redox stability of moissanite (SiC) compared with metal-metal oxide buffers at 1773 K and at pressures up to 90

- kbar. *Neues Jahrb Für Mineral Abhandlungen* 172(2–3):279–307. <https://doi.org/10.1127/njma/172/1998/279>
- Vitale Brovarone A, Martinez I, Elmaleh A, Compagnoni R, Chaduteau C, Ferraris C, Esteve I (2017) Massive production of abiogenic methane during subduction evidenced in metamorphosed ophi-carbonates from the Italian Alps. *Nat Commun* 8:14134. <https://doi.org/10.1038/ncomms14134>
- Wagner W, Pruß A (2002) The IAPWS formulation 1995 for the thermodynamic properties of ordinary water substance for general and scientific use. *J Phys Chem Ref Data* 31(2):387–535. <https://doi.org/10.1063/1.1461829>
- Walker R (2009) Highly siderophile elements in the earth, moon and mars: update and implications for planetary accretion and differentiation. *Chem Erde* 69(2):101–125. <https://doi.org/10.1016/j.chemer.2008.10.001>
- Walther J, Orville P (1983) The extraction-quench technique for determination of the thermodynamic properties of solute complexes: application to quartz solubility in fluid mixtures. *Am Mineral* 68(7–8):731–741
- Williams H, Wood B, Wade J, Frost D, Tuff J (2012) Isotopic evidence for internal oxidation of the Earth's mantle during accretion. *Earth Planet Sci Lett* 321–322:54–63. <https://doi.org/10.1016/j.epsl.2011.12.030>
- Woodland A, Koch M (2003) Variation in oxygen fugacity with depth in the upper mantle beneath the Kaapvaal craton. *Southern Africa Earth Planet Sci Lett* 214(1–2):295–310. [https://doi.org/10.1016/S0012-821X\(03\)00379-0](https://doi.org/10.1016/S0012-821X(03)00379-0)
- Wu S, Audétat A, Jochum K, Wang H, Chen J, Stoll B, Zhang C, Bao Z, Yang S, Li C, Wang X, Xu C, Xu L, Huang C, Xie L, Yang Y, Yang J (2022) three natural andesitic to rhyolitic glasses (OJY-1, OH-1, OA-1) as reference materials for in situ microanalysis. *Geostand Geoanal Res*. <https://doi.org/10.1111/ggr.12449>
- Yang X, Keppler H, Li Y (2016) Molecular hydrogen in mantle minerals. *Geochem Perspect Lett* 2(2):160–168. <https://doi.org/10.7185/geochemlet.1616>
- Yaxley G, Berry A, Kamenetsky V, Woodland A, Golovin A (2012) An oxygen fugacity profile through the Siberian Craton - Fe K-edge XANES determinations of Fe<sup>3+</sup>/Σ Fe in garnets in peridotite xenoliths from the Udachnaya East kimberlite. *Lithos* 140–141:142–151. <https://doi.org/10.1016/j.lithos.2012.01.016>
- Zhang C, Duan Z (2009) A model for C-O-H fluid in the Earth's mantle. *Geochim Cosmochim Acta* 73(7):2089–2102. <https://doi.org/10.1016/j.gca.2009.01.021>
- Zhang R, Yang J-S, Ernst W, Jahn B, Iizuka Y, Guo G (2016) Discovery of in situ super-reducing, ultrahigh-pressure phases in the Luobusa ophiolitic chromitites, tibet: new insights into the deep upper mantle and mantle transition zone. *Am Mineral* 101(6):1285–1294. <https://doi.org/10.2138/am-2016-5436>

**Publisher's Note** Springer Nature remains neutral with regard to jurisdictional claims in published maps and institutional affiliations.